frontiers in Materials

ORIGINAL RESEARCH
published: 22 October 2020
doi: 10.3389/fmats.2020.566336

Corrosion of Al(Co)CrFeNi High-Entropy Alloys

Elżbieta M. Godlewska[1], Marzena Mitoraj-Królikowska[1], Jakub Czerski[1], Monika Jawańska[1], Sergej Gein[2] and Ulrike Hecht[2]*

[1]AGH University of Science and Technology, Faculty of Materials Science and Ceramics, Kraków, Poland, [2]Access V., Aachen, Germany

High-entropy alloys, $AlCrFe_2Ni_2Mo_x$ (x = 0.00, 0.05, 0.10, and 0.15), AlCoCrFeNi, and two quinary alloys with compositions close to its face-centered cubic and body-centered cubic component phases, are tested for corrosion resistance in 3.5 wt% NaCl. The materials with different microstructure produced by arc melting or ingot metallurgy are evaluated by several electrochemical techniques: measurements of open circuit voltage, cyclic potentiodynamic polarization, and electrochemical impedance spectroscopy. Microstructure, surface topography, and composition are systematically characterized by scanning electron microscopy and energy-dispersive x-ray spectroscopy. The results indicate that minor additions of Mo positively affect corrosion resistance of the $AlCrFe_2Ni_2$ alloy by hampering pit formation. The face-centered cubic phase in the equimolar alloy, AlCoCrFeNi, is proved to exhibit more noble corrosion potential and pitting potential, lower corrosion current density and corrosion rate than the body-centered cubic phase. Overall behavior of the investigated alloys is influenced by the manufacturing conditions, exact chemical composition, distribution of phases, and occurrence of physical defects on the surface.

Keywords: high-entropy alloys, microstructure, corrosion resistance, sodium chloride, electrochemical measurements

OPEN ACCESS

Edited by:
Antonio Caggiano, Darmstadt University of Technology, Germany

Reviewed by:
Wislei Riuper Osório, Campinas State University, Brazil
Solomon M. Moses, King Fahd University of Petroleum and Minerals, Saudi Arabia

****Correspondence:***
Elżbieta Godlewska
godlewsk@agh.edu.pl

Specialty section:
This article was submitted to Structural Materials, a section of the journal Frontiers in Materials

Received: *27 May 2020*
Accepted: *02 September 2020*
Published: *22 October 2020*

Citation:
Godlewska EM, Mitoraj-Królikowska M, Czerski J, Jawańska M, Gein S and Hecht U (2020) Corrosion of Al(Co)CrFeNi High-Entropy Alloys. Front. Mater. 7:566336. doi: 10.3389/fmats.2020.566336

INTRODUCTION

The notion of high-entropy alloys (HEAs) or more generally high-entropy materials was coined quite recently and immediately awoke enormous interest by providing pathways for the development of new materials or improvement of the existing ones. In the group of high-entropy alloys, initial efforts were directed on combinations of Al with 3d transition metals, namely, Cr, Fe, Co, Ni, and to a lesser extent Cu and Mn (Miracle and Senkov, 2016). At present, the multi-principal element alloys are referred to as HEAs or compositionally complex alloys even when their configurational entropy is not high enough to secure stability of a single solid solution. Commonly, second phases are formed, including either solid solutions or intermetallics or both, which are accompanied by strong segregation of alloying elements (Pickering and Jones, 2016). AlCoCrFeNi alloys are known to have different phase composition depending on the concentration of Al. As the concentration of Al increases, their structure transforms from face-centered cubic (FCC) through mixed FCC + body-centered cubic (BCC) to BCC (Zhang et al., 2014). Since mechanical properties, that is, ductility and strength, of a number of single-phase HEAs did not meet basic requirements for structural applications, major developments were switched toward the design and fabrication of dual phase FCC + BCC alloys. One of the promising results of this work was $AlCoCrFeNi_{2.1}$, a castable eutectic high-entropy alloy with very good combination of high fracture strength and ductility (Lu et al.,

2015). This composition was further modified to Co-free $AlCrFe_2Ni_2$, which not only had mechanical properties outperforming as-cast HEAs and many titanium alloys at room temperature but also was less expensive. The structure of this alloy, consisting of FCC(A1), disordered BCC(A2), and ordered BBC(B2), results from spinodal decomposition of the original BCC phase upon cooling. The very attractive combination of fracture strength and ductility, characteristic of this alloy, is attributed to the coexistence of harder BCC phases and softer FCC (Dong et al., 2016). In addition to mechanical testing, many HEAs were tested for corrosion resistance in different aqueous environments, mostly in 3.5 wt.% NaCl and 0.1 M H_2SO_4 (Hsu et al., 2005; Lee et al., 2008b; Chou et al., 2010; Kao et al., 2010; Lin and Tsai, 2011; Qiu et al., 2017). The results looked very promising. It was indicated, however, that some alloying additions, such as Al, Cu, or Mo, could induce elemental segregation in HEAs, leading to galvanic coupling or local breakdown of passive films formed on alloy surface in salt or acid solutions. One way to overcome this drawback is seen in microstructure refining by an adequate design of manufacturing processes (Shi et al., 2017). Among the alloying additions, Mo deserves special attention since it is known to reduce the susceptibility of stainless steels to pitting corrosion. It is also known that Mo concentration in steels should be possibly low to avoid precipitation of brittle sigma and alpha phases. Simultaneous depletion in Mo and Cr of the neighboring grains would make them more vulnerable to corrosion attacks (Park and Lee, 2014; Shang et al., 2018; Valeriano et al., 2019). Although the pitting corrosion equivalent used for stainless steels cannot be simply transferred to HEAs, it was reported that small additions of Mo increased pitting corrosion resistance of some HEAs in chloride-containing environments (Chou et al., 2010; Rodriguez et al., 2018).

In this work, corrosion of selected HEAs was investigated in aqueous solutions of sodium chloride. The principal objectives were 1) to verify a hypothesis about different corrosion behavior of alloys with the same nominal composition and different microstructure on the basis of an $AlCrFe_2Ni_2$ alloy produced by different manufacturing routes, 2) to assess whether or not minor additions of Mo can positively affect the corrosion resistance of the baseline alloy, $AlCrFe_2Ni_2$, and 3) to evaluate the susceptibility to corrosion of the FCC and BCC phases in the equimolar alloy, AlCoCrFeNi. A duplex stainless steel EN 1.4517 with excellent corrosion resistance was used as a reference material.

MATERIALS AND METHODS

Experimental alloys, $AlCrFe_2Ni_2$ (with and without Mo) and AlCoCrFeNi (equimolar and with compositions close to its FCC and BCC constituent phases), were obtained from elemental powders (alloys with Co) or granules by arc melting under an argon atmosphere. Purity of the components was: Al 4N; Co 3N; Cr 3N5; Fe 3N; Ni 3N7; Mo 2N8. The reference materials, EN 1.4519 stainless steel, and two Co-free baseline alloys (purity of components: Al 2N5; Cr 2N8; Fe 3N; Ni 2N85) were produced by ingot metallurgy (Otto Junker GmbH). Alloy marked $AlCrFe_2Ni_2$ (1) was cast in air and $AlCrFe_2Ni_2$ (2) in argon. Chemical compositions of all investigated alloys are collected in **Table 1**. The EN 1.4517 duplex stainless steel (STS) had the following composition in wt.%: Fe 61.77; Cr 25.18; Ni 5.70; Cu 3.00; Mo 2.74; Si 0.85; Mn 0.53; N 0.156; V 0.032; C 0.021; P 0.002; S 0.001. Samples in the form of flat plates were ground with abrasive papers up to ISO/FEPA 1200 grit and cleaned with isopropanol. For electrochemical measurements, copper wire connections were attached to each sample using conductive silver lacquer (Leitsilber 200N, Hans Wolbring GmbH). Next, the samples were mounted in epoxy resin (Crystalline 940). Potentiodynamic and electrochemical impedance spectroscopy measurements were done in a three-electrode cell: sample as working electrode (exposed area mostly about 1 cm^2), saturated calomel electrode (SCE) as reference, and graphite as auxiliary electrode (area about 50 cm^2), using SP-150 potentiostat controlled by Bio-Logic EC-lab V11.25 or Nova 2.1.4 Metrohm Autolab B.V. (electrochemical impedance spectroscopy) software. Liquid medium used in this work was 3.5 wt.% NaCl (at 25°C). Long-term (72 h) or short-term (2 h) open circuit voltage measurements in 3.5 wt.% NaCl were conducted for all samples. Potentiodynamic measurements were done in a regular range between −300 and +300 mV vs. open circuit voltage (OCV) (polarization resistance) and in an extended potential range between −300 and +1,500 mV vs. OCV (cyclic potentiodynamic polarization test according to ASTM G61-86). Polarization resistance measurements were done at a potential scan rate of 30 mV/min and consisted of 20 cycles. Each cycle was preceded by monitoring the variations of OCV for 2 h (before the first cycle) and for 30 min (before cycles 2–20). Cyclic potentiodynamic polarization tests were conducted at a scan rate of 10 mV/min until potential reached +1,500 mV vs. OCV or until current density reached 5 mA/cm^2. Then, the reverse scan was activated and continued to the initial OCV value. As previously reported (Zhang et al., 2009), potential scan rate plays an important role in minimizing the effects of distortion of the potentiodynamic polarization curves in the analyses of Tafel slopes and corrosion current density. It is noteworthy that at the selected scan rate of 10 mV/min, no significant distortions were produced. Electrochemical impedance spectroscopy measurements were carried out in the frequency range of 10 mHz–100 kHz in a single-sine excitation mode. The

TABLE 1 | Composition of samples.

Materials	Nominal composition in at.%					
	Al	Cr	Fe	Ni	Mo	Co
$AlCrFe_2Ni_2$	16.7	16.7	33.3	33.3	–	–
$AlCrFe_2Ni_2$ (1)	16.7	16.7	33.3	33.3	–	–
$AlCrFe_2Ni_2$ (2)	16.7	16.7	33.3	33.3	–	–
$AlCrFe_2Ni_2Mo_{0.05}$	16.5	16.5	33.1	33.1	0.8	–
$AlCrFe_2Ni_2Mo_{0.10}$	16.4	16.4	32.8	32.8	1.6	–
$AlCrFe_2Ni_2Mo_{0.15}$	16.3	16.3	32.5	32.5	2.4	–
AlCoCrFeNi	20.0	20.0	20.0	20.0	–	20.0
FCC	3.1	38.8	27.7	7.8	–	22.6
BCC	33.9	5.0	13.4	28.5	–	19.2

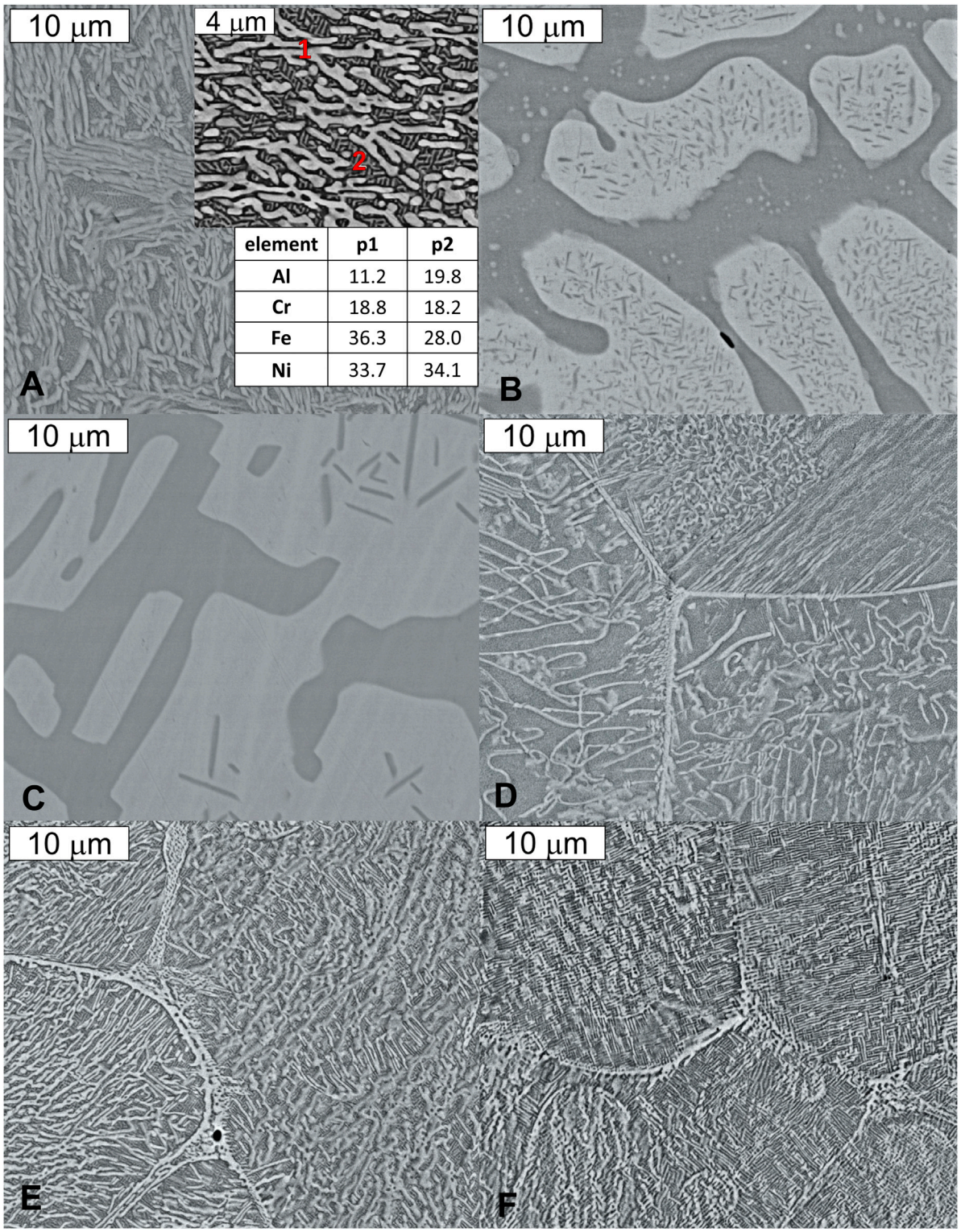

FIGURE 1 | Microstructures of $AlCrFe_2Ni_2$ **(A)**, $AlCrFe_2Ni_2$ (1) **(B)**, $AlCrFe_2Ni_2$ (2) **(C)**, $AlCrFe_2Ni_2Mo_{0.05}$ **(D)**, $AlCrFe_2Ni_2Mo_{0.10}$ **(E)**, and $AlCrFe_2Ni_2Mo_{0.15}$ **(F)**.

potential start point was the last value recorded in the 2-h OCV measurement. Three points for each frequency were recorded, and the number of points per decade was 10 in logarithmic spacing. Each sample and each type of experiment were repeated several times to assess reproducibility of the corrosion parameters. For clarity, the averaged values are presented on

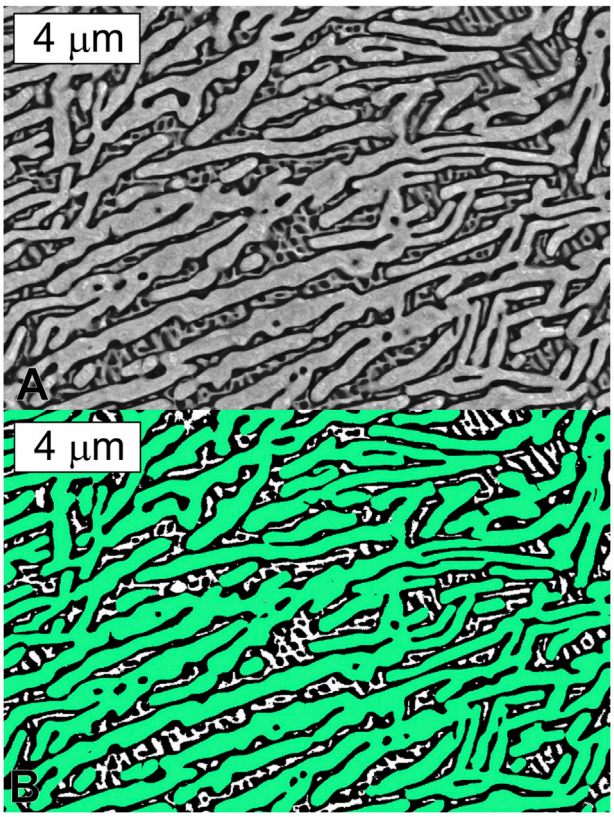

FIGURE 2 | SEM micrograph [backscattered electrons mode (BSE)] **(A)** and image segmentation **(B)** for phase analysis using the software ImageJ; segmented image colors: green—face-centered cubic (FCC), white—body-centered cubic (BCC)(A2), and black—BCC(B2).

diagrams. Sample surfaces or cross-sections before and after the tests were examined by means of a Nova NanoSEM 200 FEI scanning electron microscope (SEM) equipped with an energy-dispersive X-ray spectroscope for chemical analysis. Selected samples were analyzed by transmission electron microscopy (TEM) using a FEI Tecnai TF20 X-TWIN (FEG) microscope, equipped with an EDAX energy dispersive X-ray detector, at an accelerating voltage of 200 kV. Thin foils were prepared by a focused ion beam (FIB) technique, using a FEI Quanta 200 3D Dual Beam FIB/SEM system equipped with an Omniprobe micromanipulator.

RESULTS

Microstructure and Phase Composition

Microstructures of the $AlCrFe_2Ni_2Mo_x$ (x = 0.00, 0.05, 0.10, and 0.15) alloys are shown in **Figure 1**. The SEM image in **Figure 1A** reveals distribution of phases in the baseline alloy, $AlCrFe_2Ni_2$, obtained by arc melting. Phase separation within the grains is distinctly visible with a disordered vermicular FCC phase and a characteristic geometric pattern of very finely dispersed BCC/B2 phases resulting from spinodal decomposition (inset). Based on the results of energy-dispersive X-ray spectroscopy (EDS) analysis, the vermicular phase—marked 1 in the inset—is enriched in Fe and Cr. The two-phase region marked 2 in the inset is enriched in Al and Ni. Minor additions of Mo did not affect the phase composition of the alloy but slightly refined its microstructure, as shown in **Figures 1D,E,F**. Phase fractions in the as-cast alloy $AlCrFe_2Ni_2$ + 1.9 at.% Mo determined by image analysis (**Figures 2A,B**) on several SEM-BSE images were the following in area %: FCC(A1) 55.9 ± 1.3, BCC(B2) 35.5 ± 2.1, and BCC(A2) 8.5 ± 2.0. Micrographs in **Figures 1B,C** present samples produced by ingot metallurgy in air $AlCrFe_2Ni_2$ (1) and in argon $AlCrFe_2Ni_2$ (2). The microstructures are similar with distinctly separated grains composed of FCC and BCC phases. Some second-phase dispersions within the grains do not resemble the intricate patterns originating from spinodal decomposition.

The equimolar alloy, AlCoCrFeNi, consists of FCC and BCC phases in a layout typical of spinodal decomposition (**Figure 3A**). According to EDS analyses, Al and Ni favor the formation of BCC structures (dark gray) while Fe, Cr, and Co favor the formation of FCC structures (light gray). The images in **Figures 3B,C** present microstructures of the two alloys with average compositions corresponding roughly to the BCC and FCC components of the equimolar alloy. In both alloys, there is some amount of the second phase. Alloy denoted as FCC is composed of two Cr-rich phases, as illustrated by transmission electron microscopy images and EDS analysis in **Figure 3D**. X-ray and electron diffraction patterns confirming the structure of predominant phases in the investigated alloys are shown in **Figure 4**.

Open Circuit Voltage

The results of OCV measurements of the Co-free alloys in 3.5 wt% NaCl solution are presented in **Figure 5A**. The most noble (highest) values were recorded for the arc-melted samples $AlCrFe_2Ni_2$ and $AlCrFe_2Ni_2Mo_{0.05}$; however, in both cases, local fluctuations of potential took place. For STS, $AlCrFe_2Ni_2Mo_{0.15}$, and $AlCrFe_2Ni_2Mo_{0.10}$, the fluctuations were less pronounced. $AlCrFe_2Ni_2$ (1), cast in air, had the lowest OCV values. $AlCrFe_2Ni_2$ (2), cast in argon, behaved similarly during first 36 h, and then its potential increased to reach the final value close to those of the best arc-melted alloys containing Mo and STS. All Co-free alloys under investigation exhibited a low spread of OCV values and quick stabilization.

The OCV variations over time for the equimolar alloy, AlCoCrFeNi, and two quinary alloys denoted as BCC and FCC are presented in **Figure 5B** on the background of the STS reference. The values of potential are more negative for all three alloys compared with STS, and all curves are relatively smooth. The lowest OCV values were recorded for the BCC sample, i.e., one rich in Al and Ni. The Cr-rich FCC sample showed OCV values closest to those of STS.

Cyclic Potentiodynamic Polarization

Variations of polarization resistance (Rp) over 20 consecutive cycles of potentiodynamic measurements for all the Co-free alloys and STS reference are presented in **Figure 6A**. Generally, the fluctuating Rp values revealed an increasing trend: the highest on average (up to about 4 MΩ cm^2) being recorded

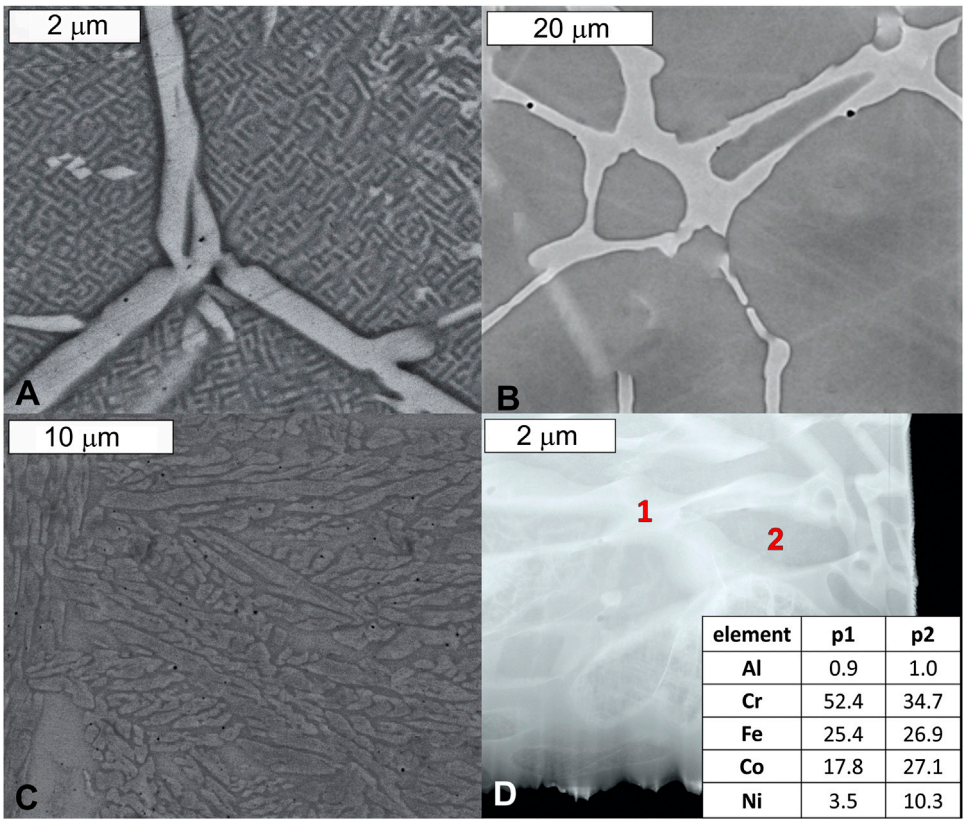

element	p1	p2
Al	0.9	1.0
Cr	52.4	34.7
Fe	25.4	26.9
Co	17.8	27.1
Ni	3.5	10.3

FIGURE 3 | Microstructures of AlCoCrFeNi **(A)** and two quinary alloys with compositions close to its major component BCC **(B)** and FCC **(C,D)**; SEM **(A–C)**, STEM **(D)**, EDS analysis (at.%) in marked points.

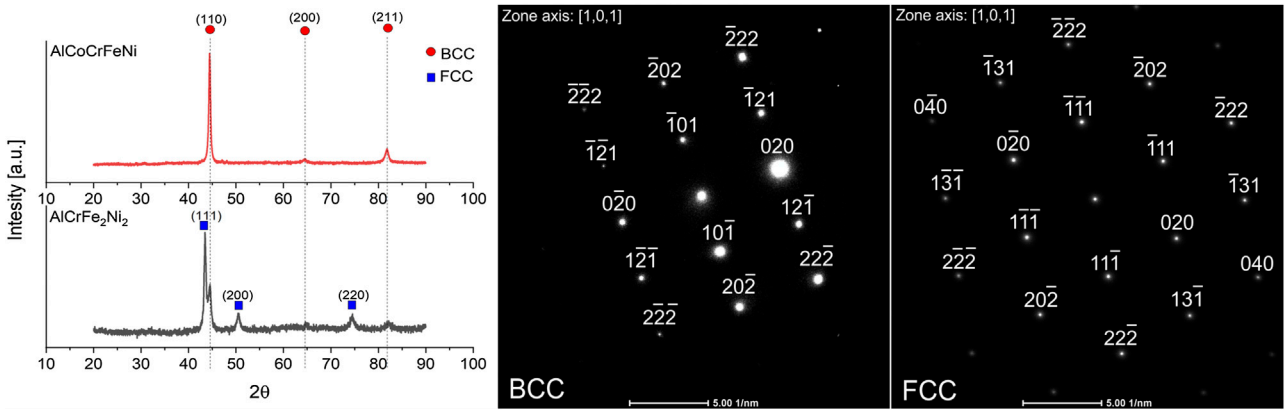

FIGURE 4 | X-ray **(A)** and electron **(B)** diffraction patterns confirming the occurrence of predominant phases in the investigated alloys.

for $AlCrFe_2Ni_2$ and the lowest (up to about 800 kΩ cm^2) for $AlCrFe_2Ni_2Mo_{0.05}$. STS behaved in a more regular manner, but the recorded R*p* values were lower, reaching about 1.5 MΩ cm^2 at the most.

The results of similar measurements for the three alloys containing Co and the STS reference are presented in **Figure 6B**. Compared with STS, the quinary alloy, FCC, rich in Cr and Fe, had higher polarization resistance over 20 cycles of potentiodynamic measurements, approaching 4 MΩ cm^2 at the end of the experiment. The AlCoCrFeNi and BCC samples showed irregular variations of polarization resistance in consecutive cycles, with fluctuations around the values

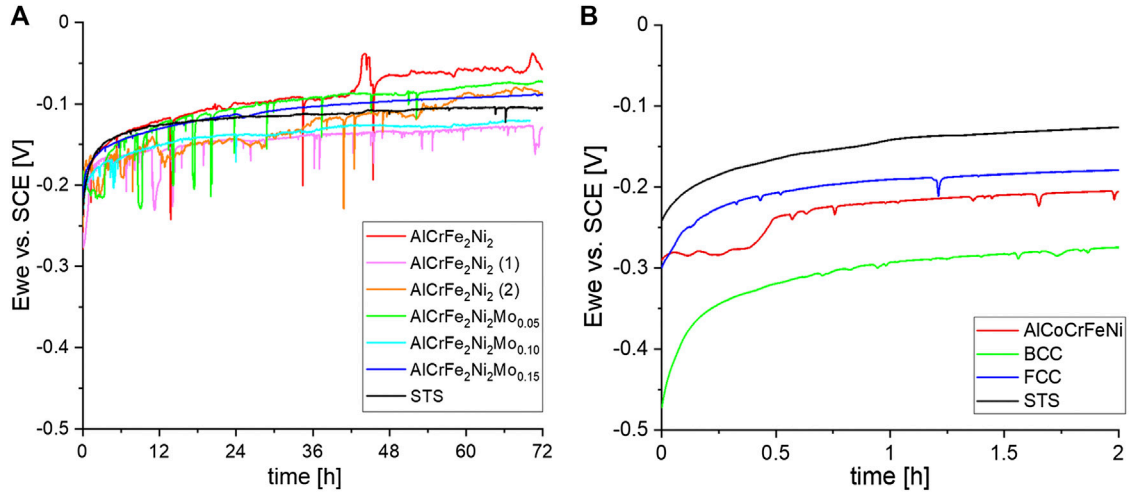

FIGURE 5 | Open circuit voltage evolution over time in 3.5 wt.% NaCl for the Co-free alloys and stainless steel (STS) **(A)**, and for three quinary alloys and STS **(B)**.

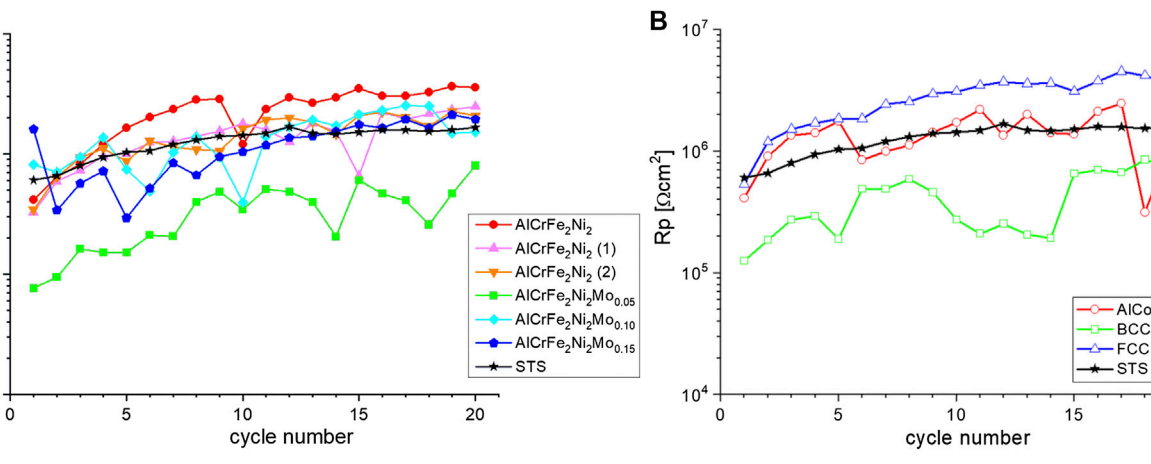

FIGURE 6 | Variations of polarization resistance over 20 consecutive cycles in 3.5 wt.% NaCl for Co-free alloys and STS **(A)**, and for three quinary alloys and STS **(B)**.

recorded for STS in the former case and the lowest values, not exceeding 900 kΩ cm^2, in the latter case.

Tafel polarization curves of the $AlCrFe_2Ni_2Mo_x$ alloys are collected in **Figure 7A**. Compared with the baseline alloy, all other HEAs showed worse corrosion properties, reflected in higher corrosion currents (i_{corr}) and corrosion rates, as illustrated in **Table 2**. Pitting potential was clearly visible only in the case of arc-melted $AlCrFe_2Ni_2$, $AlCrFe_2Ni_2Mo_{0.15}$, and STS. Unlike other alloys, STS exhibited a very wide passivation range and repassivated during the reverse scan. All alloys in this series, except $AlCrFe_2Ni_2Mo_{0.05}$, had corrosion currents lower than 0.1 μA/cm^2.

Tafel plots for AlCoCrFeNi, BCC, FCC, and STS are shown in **Figure 7B**. The polarization curves of FCC and STS are very similar, with a pitting potential (E_{pit}) close to 1.0 V (**Table 2**). However, the repassivation potentials (E_{pass}) were significantly different: −0.13 V for FCC and +0.83 V for STS (**Figure 7B**). According to the data in **Table 2**, the most negative value of E_{pit} was recorded for the BCC sample. Corrosion potentials (E_{corr}) of the investigated alloys ranged between −0.20 and −0.28 V. The least negative E_{corr} (−0.14 V) was recorded for STS and the most negative (equal or lower than −0.30 V) for AlCoCrFeNi and BCC. Current density of 5 mA/cm^2 was reached, and reverse scan was started at potentials (E_{rev}) 0.12–0.15 V ($AlCrFe_2Ni_2Mo_x$ and BCC), 0.16–0.19 V ($AlCrFe_2Ni_2$ and AlCoCrFeNi), and 1.0 V (STS and FCC). The highest corrosion current (i_{corr}) as well as corrosion rate was measured for BCC, $AlCrFe_2Ni_2Mo_{0.05}$, and AlCoCrFeNi.

Electrochemical Impedance Spectroscopy

The results of electrochemical impedance spectroscopy measurements are presented in a form of a Nyquist plot for

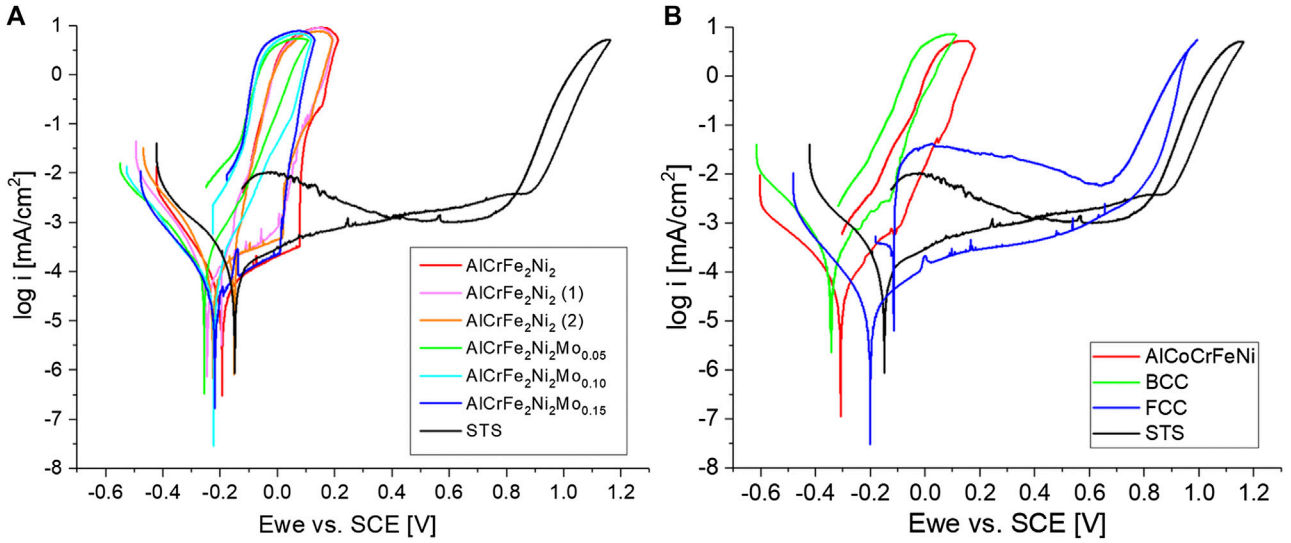

FIGURE 7 | Potentiodynamic polarization curves (Tafel) in 3.5 wt% NaCl for the Co-free alloys and STS **(A)**, and for three quinary alloys and STS **(B)**.

TABLE 2 | Parameters obtained from Tafel plots in **Figures 7A,B**.

Materials	E_{corr} (V)	E_{pit} (V)	E_{rev} (V)	i_{corr} (μA/cm^2)	Corrosion rate (mmpy)
AlCrFe$_2$Ni$_2$	−0.25 ± 0.01	0.07 ± 0.01	0.19 ± 0.02	0.049 ± 0.022	(4.2 ± 0.8) × 10^{-4}
AlCrFe$_2$Ni$_2$ (1)	−0.25 ± 0.01	−0.03 ± 0.01	0.18 ± 0.02	0.052 ± 0.004	(4.9 ± 0.4) × 10^{-4}
AlCrFe$_2$Ni$_2$ (2)	−0.28 ± 0.00	0.00 ± 0.02	0.16 ± 0.00	0.074 ± 0.001	(7.1 ± 0.0) × 10^{-4}
AlCrFe$_2$Ni$_2$Mo$_{0.05}$	−0.27 ± 0.01	–	0.13 ± 0.03	0.166 ± 0.041	(15.8 ± 3.9) × 10^{-4}
AlCrFe$_2$Ni$_2$Mo$_{0.10}$	−0.28 ± 0.00	–	0.14 ± 0.04	0.099 ± 0.003	(8.0 ± 2.1) × 10^{-4}
AlCrFe$_2$Ni$_2$Mo$_{0.15}$	−0.26 ± 0.00	0.02 ± 0.02	0.15 ± 0.03	0.059 ± 0.017	(5.5 ± 1.6) × 10^{-4}
AlCoCrFeNi	−0.30 ± 0.03	–	0.16 ± 0.02	0.116 ± 0.066	(10.2 ± 6.0) × 10^{-4}
BCC	−0.34 ± 0.01	−0.07 ± 0.08	0.12 ± 0.01	0.141 ± 0.046	(13.6 ± 6.3) × 10^{-4}
FCC	−0.20 ± 0.05	0.83 ± 0.05	1.00 ± 0.02	0.022 ± 0.002	(1.9 ± 0.2) × 10^{-4}
STS	−0.14 ± 0.01	0.89 ± 0.01	1.16 ± 0.01	0.040 ± 0.028	(3.9 ± 2.7) × 10^{-4}

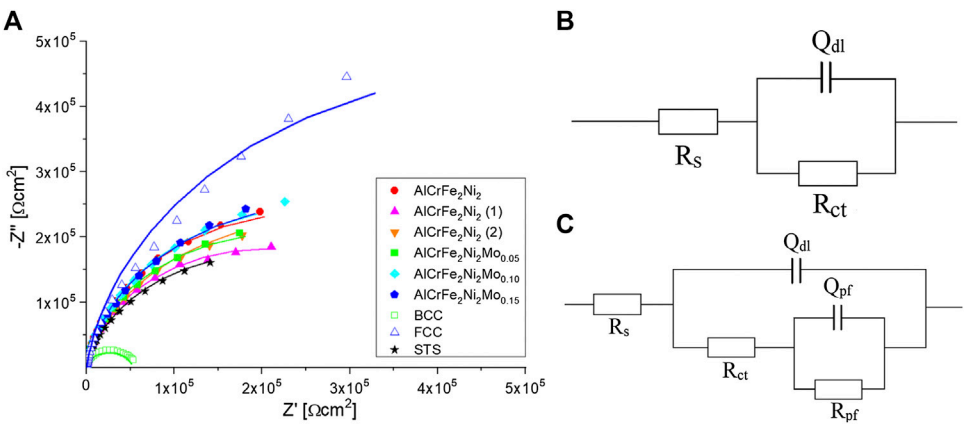

FIGURE 8 | Nyquist plot **(A)** and fitted equivalent electrochemical circuits for all high entropy alloys **(B)**, and STS **(C)**.

TABLE 3 | Fitted parameters for the elements of equivalent circuits.

Sample	R_s (Ω cm^2)	Q_{dl} (μF/cm^2)	n (–)	R_{ct} (kΩ cm^2)	Q_{pf} (μF/cm^2)	n (–)	R_{pf} (kΩ cm^2)	χ^2
$AlCrFe_2Ni_2$	7 ± 0	40 ± 1	0.95 ± 0.01	520 ± 14	–	–	–	0.0410 ± 0.0088
$AlCrFe_2Ni_2$ (1)	9 ± 1	39 ± 8	0.92 ± 0.01	413 ± 24	–	–	–	0.0414 ± 0.0252
$AlCrFe_2Ni_2$ (2)	7 ± 1	44 ± 3	0.89 ± 0.03	537 ± 24	–	–	–	0.0480 ± 0.0330
$AlCrFe_2Ni_2Mo_{0.05}$	6 ± 0	40 ± 1	0.94 ± 0.01	459 ± 34	–	–	–	0.0306 ± 0.0093
$AlCrFe_2Ni_2Mo_{0.10}$	6 ± 0	35 ± 1	0.93 ± 0.01	550 ± 60	–	–	–	0.0215 ± 0.0056
$AlCrFe_2Ni_2Mo_{0.15}$	5 ± 0	32 ± 0	0.92 ± 0.01	573 ± 17	–	–	–	0.0428 ± 0.0134
BCC	6 ± 0	6 ± 0	0.91 ± 0.00	53 ± 0.00	–	–	–	0.0827 ± 0.0004
FCC	9 ± 1	18 ± 0	0.92 ± 0.03	1,039 ± 80	–	–	–	0.1423 ± 0.0327
STS	8 ± 1	41 ± 1	0.91 ± 0.00	275 ± 21	20 ± 1	0.72 ± 0.03	125 ± 7	0.0164 ± 0.0030

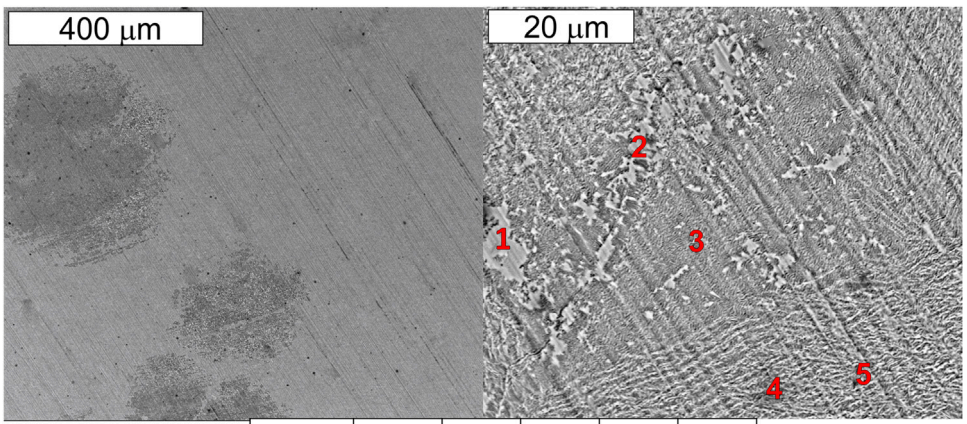

element	p1	p2	p3	p4	p5
Al	10.6	11.0	1.8	4.5	4.4
Cr	16.3	17.3	28.3	21.5	25.1
Fe	33.5	35.0	52.3	46.4	45.0
Ni	38.3	35.2	14.6	25.3	23.6
Mo	1.3	1.5	3.1	2.3	1.9

FIGURE 9 | Surface of an $AlCrFe_2Ni_2Mo_{0.10}$ sample after potentiodynamic polarization test (Tafel) in 3.5 wt% NaCl and EDS analysis (at.%) in marked points.

all the investigated alloys and the STS reference in **Figure 8A**. The related equivalent electrical circuits are shown in **Figures 8B,C**, and the fitted parameters are listed in **Table 3**. The behavior of all samples except STS was described by a simple Randles circuit. A more complex equivalent circuit was proposed for STS, based on the study by Pan et al. (1998) and Mahato and Singh (2011) and the best fitting parameters. In all cases, a constant phase element was selected representing a non-ideal capacitor in order to take account of surface roughness and inhomogeneities, that is, varying surface energy, which affect the reaction rates. Thus, Q_{dl} and Q_{pf} indicate impedances described as constant phase element, CPE = $[Q(i\,\omega)^n]^{-1}$, where Q is the capacitance, $i = (-1)^{0.5}$, ω is the angular frequency, and $-1 \leq n \leq 1$, as previously reported (Osório et al., 2013; Kumar et al., 2017; Rodrigues et al., 2020). The values of solution resistance (R_s) were in the range of 5.0–9.0 Ωcm^2. The values of charge transfer resistance (R_{ct}) for the Co-free samples were between 413 and 573 kΩ cm^2, the highest one being recorded for $AlCrFe_2Ni_2Mo_{0.15}$. For STS, the R_{ct} value was much lower, equal to 275 kΩ cm^2. The relatively low R_{ct} value for STS was probably connected with the occurrence of a protective film characterized by an additional resistance R_{pf} = 125 kΩ cm^2. The electrical double layer capacitance (Q_{dl}) ranged from 32 to 44 μF/cm^2. In the series of quinary alloys, some of the fitted parameters did not fall in the same range, e.g., charge transfer resistance of FCC exceeded 1 MΩ cm^2 but that of BCC was merely 64 kΩ cm^2. The electrical double layer capacitance for FCC and BCC was 18 and 6 μF/cm^2, respectively. The values for AlCoCrFeNi were not quoted in **Table 3** because of poor reproducibility. Although the goodness of fit (χ^2) evaluated by the NOVA 2.1.4. Metrohm Autolab B.V. software for the selected equivalent circuits was not sufficient, some differences in corrosion behavior and tendencies could be deduced from the obtained data.

Typical surface damages of the investigated alloys in 3.5 wt% NaCl solutions after potentiodynamic polarization test are shown in **Figure 9**. In this environment, the dominant corrosion type is pitting corrosion, as evidenced by darker round-shaped areas. The EDS analyses in selected spots on the surface (**Figure 9**)

indicated depletion in Al and Ni (points 3, 4, and 5) compared with the neighboring areas which preserved chemical composition of the FCC phase (points 1 and 2).

DISCUSSION

It has been evidenced by many studies that mechanical properties of HEAs depend on the microstructure (Tang et al., 2013, Tang et al., 2015; Wang et al., 2018). Rapidly solidifying alloys produced by arc melting or additive manufacturing are generally nanostructured, and their nano-sized components are responsible for the dispersion strengthening effect. Subsequent processing, for example, heat treatments, may, however, lead to grain coarsening and loss of superb properties.

Very impressive differences in microstructure were visible in $AlCrFe_2Ni_2$ alloys produced by arc melting and ingot metallurgy. The distribution of phases in the baseline alloy, $AlCrFe_2Ni_2$, obtained by arc melting (**Figure 1A**) was practically the same as that earlier described by Dong et al. (2016), with characteristic vermicular FCC and nanostructured BCC phases, while in cast alloys with the same chemical composition, the nanostructures were absent, and grains were much coarser.

The results of several electrochemical tests carried out in this work indicate that there is a noticeable influence of grain size and distribution of phases on the exposed surface on the corrosion behavior. In the OCV measurements, the trends were similar for the three $AlCrFe_2Ni_2$ samples, that is, the potential increased with time, but the values recorded for the arc-melted material were less negative than those recorded for both cast ones. Numerous spikes on the OCV curves generally reflect local phenomena (pitting), such as damage of a protective layer by ions in the solution (Kabir and Mahmud, 2011). Polarization resistance describes the ability to resist the electron transfer from one phase to another. Values increasing over time suggest improvement of the corrosion resistance. The average values of polarization resistance over 20 consecutive cycles were higher for the arc-melted alloy than those for the cast ones. Significant scatter of the experimental points in consecutive cycles indicates that protective layers formed on alloy surfaces were not stable enough. Tafel polarization curves were very similar in shape, and again some of the derived characteristic parameters, such as corrosion current, pitting potential, and corrosion rate, listed in **Table 2**, were more advantageous for the arc-melted sample. The differences in corrosion behavior can be attributed to different relative areas of individual phases and density of grain/phase boundaries on the surface exposed to the solution, especially when some phases are more reactive than others, as is evidenced by depletion of the BCC phase in aluminum and nickel.

Chloride ions are known to interact with the native oxide films, leading to their breakdown, particularly in the areas where these films are thinner, for example, over intermetallic precipitates in Al-based alloys (Shao et al., 2003; Yasakau et al., 2006; Shi et al., 2017). Failure of the oxide barrier triggers chemical reactions of active metals, such as aluminum, with water, accompanied by the evolution of hydrogen:

$$2Al + 6H_2O = 2Al^{3+} + 6OH^- + 3H_2\uparrow.$$

Susceptibility of the exposed grains to pitting corrosion is also dependent on their crystallographic orientation - crystallographic planes with higher atomic density, higher coordination number, and lower surface energy are expected to be naturally more resistant (Shahryari et al., 2009). As it has been illustrated by numerous examples (Ralston et al., 2010), the reduced grain size has positive effects on corrosion rate only in cases when an oxide/passive film can form on the surface of metallic materials. Otherwise, dense grain boundaries are likely to increase surface reactivity and the corrosion rate. Also, segregation of impurities may contribute to the role of grain refinement in corrosion behavior (Miyamoto et al., 2008). Intergranular corrosion is, namely, often induced by impurity segregation and precipitation at grain boundaries. It has been reported that dilution of the segregated impurities at grain boundaries accounts for the beneficial effect of grain size reduction on corrosion resistance (Palumbo et al., 1990; Wang et al., 1993; Palumbo and Erb, 1999).

In the alloys investigated in this work, major impurities due to processing in air or argon were Al oxide or nitride particles. These might contribute to abrupt fluctuations of potential or current in electrochemical tests. There was no evidence, however, that the alloy processed in air was much more susceptible to pitting than the one processed in argon [$AlCrFe_2Ni_2$ (1) and $AlCrFe_2Ni_2$ (2), respectively]. Another issue is that all metals used for arc melting had better purity than those used for casting, and thus increased concentration of impurities in the intercrystalline regions of the coarse-grained microstructure might lead to worse corrosion resistance.

As mentioned earlier, the Mo additions contributed to some refinement of alloy microstructure. In sodium chloride solution, for the three Mo-containing alloys, the values of measured electrochemical parameters were less advantageous or comparable with the baseline arc-melted alloy. In the OCV measurements, the most striking difference was disappearance of potential spikes at the higher contents of Mo in the alloy, which suggested that local phenomena became less pronounced. In the Tafel plots, the curves shifted toward higher potentials with increasing content of Mo, and fluctuations of current were practically absent for $AlCrFe_2Ni_2Mo_{0.15}$. The values of charge transfer resistance (R_{ct}) derived from the Nyquist plot increased with the Mo content and were in a range typical of alloys with a similar composition and microstructure (Lu et al., 2015). The values of solution resistance (R_s) were similar for all the alloys and consistent with the earlier reported data (Kumar et al., 2017). The double layer capacitance (Q_{dl}) was approximately the same as reported by other researchers (Pan et al., 1998; Kumar et al., 2017). In comparison with other HEAs, such as $Al_xCrFe_{1.5}MnNi_{0.5}$ (Lee et al., 2008b),

$FeCoNiCrCu_x$ (Hsu et al., 2005) or $Co_{1.5}CrFeNi_{1.5}Ti_{0.5}Mo_x$ (Lee et al., 2008a), tested in NaCl solutions, all Co-free alloys investigated in this work had much better corrosion resistance.

Mo together with Cr in steels is very effective in preventing pitting corrosion in chloride-containing media. The exact mechanisms involved are not fully understood. It is believed that Cr and Mo oxides form barriers for the penetration of chloride ions. A number of researchers claimed that Mo in the passive layer on steels was present mostly in a form of adsorbed anions (MoO_4^{2-}), constituting a barrier against the electrochemical attack (Pourbaix, 1974; Kodama and Ambrose, 1977; Ogura and Ohama, 1984; Lu and Clayton, 1985; Brooks et al., 1986; Clayton and Lu, 1986). Mo was reported to lower the chloride ion content in the passive film on steel due to its ability to form soluble stable Mo–oxo–chloro complexes as well as insoluble chlorides and oxide chlorides on the surface (Wegrelius et al., 1999). In the case of HEAs containing aluminum in high proportions, the effect of Mo is by far less strong.

The increasing concentration of aluminum in HEAs generally leads to increased volume fraction of a BCC phase and enhancement of pitting corrosion, as illustrated by the behavior of a series of alloys, $Al_xCrFe_{1.5}MnNi_{0.5}$ (Lee et al., 2008a; Shi et al., 2017). The BCC phase with a low concentration of Cr and high concentration of Al produced porous nonprotective oxide layers in contact with a sodium chloride solution.

The detrimental role of the Al-rich component of the investigated alloys was clearly visible in electrochemical measurements conducted in 3.5 wt.% NaCl. The relative amount of the BCC phase in the equimolar quinary alloy was about 75 vol.%, while only about 40 vol.% in the Co-free baseline alloy and consequently the values of corrosion parameters were significantly worse: corrosion potential was much lower (−0.30 vs. −0.25 V), and corrosion current density was higher (0.116 vs. 0.049 $\mu A/cm^2$). The alloys denoted as BCC and FCC with compositions close to the major phases in the equimolar alloy presented very different chemical properties. The BCC alloy with the Al/Cr atomic ratio of about 7/1 had the lowest OCV, corrosion potential, and pitting potential values among all alloys investigated in this work. Compared with $AlCrFe_2Ni_2$, its corrosion current density and corrosion rate were roughly three times higher (0.141 $\mu A/cm^2$ and 13.6 × 10^{-4} mmpy, respectively). On the contrary, the alloy denoted as FCC with the reversed proportions of Al and Cr, Al/Cr atomic ratio of about 1/10, had very good corrosion resistance, comparable with the STS reference in terms of corrosion and pitting potential, corrosion current density, passivation range, and corrosion rate. It also showed exceptionally high polarization resistance and charge transfer resistance. These observations are consistent with the results previously published by other authors regarding the effects of Al, Mo, and Cr on corrosion resistance of some HEAs in aqueous environments containing chloride or sulfate species (Shi et al., 2017).

CONCLUSIONS

Electrochemical measurements in 3.5 wt% NaCl allowed formulation of the following conclusions regarding corrosion behavior of the investigated high-entropy alloys:

(1) Microstructure of the $AlCrFe_2Ni_2$ alloys determined by the manufacturing and processing conditions influenced their chemical behavior to some extent. Major role was attributed to the grain size, distribution of phases on the surface as well as amount and distribution of impurities. Nanostructures formed by spinodal decomposition contributed to the enhancement of corrosion resistance.
(2) The effect of Mo on pitting corrosion resistance was noticeable, especially at the highest concentration of this additive in the arc-melted alloys, that is, $AlCrFe_2Ni_2Mo_{0.15}$.
(3) The Al/Cr atomic ratio appeared crucial for the corrosion resistance of the investigated Al(Co)CrFeNi alloys because it conditioned formation of the Al-rich BCC phase and its susceptibility to spinodal decomposition.
(4) All experimental alloys investigated in this work, except the Cr-deficient quinary BCC, showed corrosion behavior better than many other HEAs described in the literature.
(5) The nanostructured Co-free alloy, $AlCrFe_2Ni_2$, which has been reported to have excellent combination of strength and ductility, outperformed the equimolar quinary alloy, AlCoCrFeNi, in terms of corrosion resistance owing to the higher volume fraction of the Al-deficient FCC phase.
(6) The $AlCrFe_2Ni_2$ alloy with minor addition of Mo and improved resistance to pit formation has good prospects for application.
(7) Systematic studies are underway to assess further possible improvements in corrosion resistance brought about by Mo in higher proportions also in the environments other than NaCl, and to clarify the mechanisms involved.

DATA AVAILABILITY STATEMENT

The raw data supporting the conclusions of this article will be made available by the authors, without undue reservation.

AUTHOR CONTRIBUTIONS

EG and UH provided general concept of this study, support, and supervision of experiments. MM-K, JC, and MJ were involved in planning and execution of corrosion tests, establishing the system of data collection and archiving. SG was involved in planning and execution of the arc-melting procedure, and characterization of the Co-free alloys. All authors contributed to characterization of samples at different stages of manufacturing and testing. JC wrote the first draft of the manuscript devoted to corrosion testing of the Co-free alloys. MM-K wrote the first draft on quinary alloys with Co. MM-K, JC, MJ, and EG were involved in the discussion and interpretation of experimental results as well as editing of the final version of the paper.

FUNDING

Investigations were conducted within a NADEA project (M-ERA.NET 2017) with a financial support from the National Science Centre Poland (UMO-2017/26/Z/ST8/01238). The measurements of quinary alloys were financed by the Polish Ministry of Science and Education—Subsidy No. 16.16.160.557.

ACKNOWLEDGMENTS

The authors acknowledge the contribution of M. Gajewska from the Academic Centre for Materials and Nanotechnologies, AGH UST, in Kraków PL, who performed TEM/EDS analyses of the quinary alloys, and Krzysztof Mars from the Faculty of Materials Science and Ceramics, AGH UST, who was involved in the manufacturing of these alloys.

REFERENCES

Brooks, A. R., Clayton, C. R., Doss, K., and Lu, Y. C. (1986). On the role of Cr in the passivity of stainless steel. *J. Electrochem. Soc.* 133, 2459–2464. doi:10.1149/1.2108450

Chou, Y. L., Yeh, J. W., and Shih, H. C. (2010). The effect of molybdenum on the corrosion behaviour of the high-entropy alloys Co1.5CrFeNi1.5Ti0.5Mox in aqueous environments. *Corros. Sci.* 52, 2571–2581. doi:10.1016/j.corsci.2010.04.004

Clayton, C. R., and Lu, Y. C. (1986). A bipolar model of the passivity of stainless steel: the role of Mo addition. *J. Electrochem. Soc.* 133, 2465–2473. doi:10.1149/1.2108451

Dong, Y., Gao, X., Lu, Y., Wang, T., and Li, T. (2016). A multi-component $AlCrFe_2Ni_2$ alloy with excellent mechanical properties. *Mater. Lett.* 169, 62–64. doi:10.1016/j.matlet.2016.01.096

Hsu, Y. J., Chiang, W. C., and Wu, J. K. (2005). Corrosion behavior of $FeCoNiCrCu_x$ high-entropy alloys in 3.5% sodium chloride solution. *Mater. Chem. Phys.* 92, 112–117. doi:10.1016/j.matchemphys.2005.01.001

Kabir, K. B., and Mahmud, I. (2011). Study of erosion–corrosion of stainless steel, brass and aluminum by open circuit potential measurements. *J. Chem. Eng.* 25, 13–17. doi:10.3329/jce.v25i0.7234

Kao, Y.-F., Lee, T.-D., Chen, S.-K., and Chang, Y.-S. (2010). Electrochemical passive properties of $Al_xCoCrFeNi$ (x = 0, 0.25, 0.50, 1.00) alloys in sulfuric acids. *Corros. Sci.* 52, 1026–1034. doi:10.1016/j.corsci.2009.11.028

Kodama, T., and Ambrose, J. R. (1977). Effect of molybdate ion on the repassivation kinetics of iron in solutions containing chloride ions. *Corrosion* 33, 155–161. doi:10.5006/0010-9312-33.5.155

Kumar, N., Fusco, M., Komarasamy, M., Mishra, R. S., Bourham, M., and Murty, K. L. (2017). Understanding effect of 3.5 wt.% NaCl on the corrosion of $Al_{0.1}CoCrFeNi$ high-entropy alloy. *J. Nucl. Mater.* 495, 154–163. doi:10.1016/j.jnucmat.2017.08.015

Lee, C. P., Chang, C. C., Chen, Y. Y., Yeh, J. W., and Shih, H. C. (2008a). Effect of the aluminium content of $Al_xCrFe_{1.5}MnNi_{0.5}$ high-entropy alloys on the corrosion behaviour in aqueous environments. *Corros. Sci.* 50, 2053–2060. doi:10.1016/j.corsci.2008.04.011

Lee, C. P., Chen, Y. Y., Hsu, C. Y., Yeh, J. W., and Shih, H. C. (2008b). Enhancing pitting corrosion resistance of $Al_xCrFe_{1.5}MnNi_{0.5}$ high-entropy alloys by anodic treatment in sulfuric acid. *Thin Solid Films.* 517, 1301–1305. doi:10.1016/j.tsf.2008.06.014

Lin, C.-M., and Tsai, H.-L. (2011). Evolution of microstructure, hardness, and corrosion properties of high-entropy $Al_{0.5}CoCrFeNi$ alloy. *Intermetallics* 19, 288–294. doi:10.1016/j.intermet.2010.10.008

Lu, Y. C., and Clayton, C. R. (1985). Evidence for a bipolar mechanism of passivity in Mo bearing stainless steels. *J. Electrochem. Soc.* 132, 2517–2518. doi:10.1149/1.2113614

Lu, Y., Dong, Y., Guo, S., Jiang, L., Kang, H., Wang, T., et al. (2015). A promising new class of high-temperature alloys: eutectic high-entropy alloys. *Sci. Rep.* 4, 6200. doi:10.1038/srep06200.

Mahato, N., and Singh, M. M. (2011). Investigation of passive film properties and pitting resistance of AISI 316 in aqueous ethanoic acid containing chloride ions using electrochemical impedance spectroscopy (EIS). *Port. Electrochim. Acta.* 29, 233–251. doi:10.4152/pea.201104233

Miracle, D., and Senkov, O. (2016). A critical review of high entropy alloys and related concepts. *Acta Mater.* 122, 448–511. doi:10.1016/j.actamat.2016.08.081

Miyamoto, H., Harada, K., Mimaki, T., Vinogradov, A., and Hashimoto, S. (2008). Corrosion of ultra-fine grained copper fabricated by equal-channel angular pressing. *Corros. Sci.* 50, 1215–1220. doi:10.1016/j.corsci.2008.01.024

Ogura, K., and Ohama, T. (1984). Pit formation in the cathodic polarization of passive iron IV. Repair mechanism by molybdate, chromate and tungstate. *Corrosion* 40, 47–51. doi:10.5006/1.3593909

Osório, W. R., Freitas, E. S., and Garcia, A. (2013). EIS and potentiodynamic polarization studies on immiscible monotectic Al–In alloys. *Electrochim. Acta.* 102, 436–445. doi:10.1016/j.electacta.2013.04.047

Palumbo, G., and Erb, U. (1999). Enhancing the operating life and performance of lead-acid batteries via grain-boundary engineering. *MRS Bull.* 24, 27–32. doi:10.1557/s0883769400053422

Palumbo, G., Thorpe, S. J., and Aust, K. T. (1990). On the contribution of triple junctions to the structure and properties of nanocrystalline materials. *Scr. Metall. Mater.* 24, 1347–1350. doi:10.1016/0956-716x(90)90354-j

Pan, J., Leygraf, C., Jargelius-Pettersson, R. F. A., and Linden, J. (1998). Characterization of high-temperature oxide films on stainless steels by electrochemical-impedance spectroscopy. *Oxid. Met.* 50, 431–455. doi:10.1023/A:1018856808917

Park, H.-J., and Lee, H.-W. (2014). Effect of alloyed Mo and W on the corrosion characteristics of super duplex stainless steel weld. *Int. J. Electrochem. Sci.* 9, 6687–6698.

Pickering, E. J., and Jones, N. G. (2016). High-entropy alloys: a critical assessment of their founding principles and future prospects. *Int. Mater. Rev.* 61, 183–202. doi:10.1080/09506608.2016.1180020.

Pourbaix, M. (1974). *Atlas of electrochemical equilibria in aqueous solutions*. Houston, TX: NACE.

Qiu, Y., Thomas, S., Gibson, M. A., Fraser, H. L., and Birbilis, N. (2017). Corrosion of high entropy alloys. *NPJ Mater. Degrad.* 1, 1–18. doi:10.1038/s41529-017-0009-y

Ralston, K. D., Birbilis, N., and Davies, C. H. J. (2010). Revealing the relationship between grain size and corrosion rate of metals. *Scr. Mater.* 63, 1201–1204. doi:10.1016/j.scriptamat.2010.08.035

Rodrigues, J. F. Q., Padilha, G. S., Bortolozo, A. D., and Osório, W. R. (2020). Effect of sintering time on corrosion behavior of an Ag/Al/Nb/Ti/Zn alloy system. *J. Alloys Comp.* 834, 155039. doi:10.1016/j.jallcom.2020.155039

Rodriguez, A. A., Tylczak, J. H., Gao, M. C., Jablonski, P. D., Detrois, M., Ziomek-Moroz, M., et al. (2018). Effect of molybdenum on the corrosion behavior of high-entropy alloys $CoCrFeNi_2$ and $CoCrFeNi_2Mo_{0.25}$ under sodium chloride aqueous conditions. *Adv. Mater. Sci. Eng.* 2018, 1–11. doi:10.1155/2018/3016304

Shahryari, A., Szpunar, J. A., and Omanovic, S. (2009). The influence of crystallographic orientation distribution on 316LVM stainless steel pitting behavior. *Corros. Sci.* 51, 677–682. doi:10.1016/j.corsci.2008.12.019

Shang, X.-L., Wang, Z.-J., Wu, Q.-F., Wang, J.-C., Li, J.-J., and Yu, J.-K. (2018). Effect of Mo addition on corrosion behavior of high-entropy alloys CoCrFeNiMox in aqueous environments. *Acta Metall. Sin. (Engl. Lett.)* 32, 41. doi:10.1007/s40195-018-0812-7

Shao, M., Fu, Y., Hu, R., and Lin, C. (2003). A study on pitting corrosion of aluminum alloy 2024-T3 by scanning microreference electrode technique. *Mater. Sci. Eng. A* 344, 323–327. doi:10.1016/S0921-5093(02)00445-8

Shi, Y., Yang, B., and Liaw, P. (2017). Corrosion-resistant high-entropy alloys: a review. *Metals* 7, 43. doi:10.3390/met7020043.

Tang, Z., Gao, M. C., Diao, H., Yang, T., Liu, J., Zuo, T., et al. (2013). Aluminum alloying effects on lattice types, microstructures, and mechanical behavior of high-entropy alloys systems. *JOM* 65, 1848–1858. doi:10.1007/s11837-013-0776-z

Thang, Z., Senkov, O. N., Parish, C. M., Zhang, C., Zhang, F., Santodonato, L. J., et al. (2015). Tensile ductility of an AlCoCrFeNi multi-phase high-entropy alloy through hot isostatic pressing (HIP) and homogenization. *Mater. Sci. Eng. A* 647, 229–240. doi:10.1016/j.msea.2015.08.078

Valeriano, L., Correa, E. O., Mariano, N. A., Robin, A. L. M., Machado, C., Tommaselli, M., et al. (2019). Influence of the solution-treatment temperature and short aging times on the electrochemical corrosion behaviour of Uns S32520 super duplex stainless steel. *Mat. Res.* 22, 1–7. doi:10.1590/1980-5373-2018-0774

Wang, N., Palumbo, G., Wang, Z., Erb, U., and Aust, K. T. (1993). On the persistence of four-fold triple line nodes in nanostructured materials. *Scr. Metall. Mater.* 28, 253–256. doi:10.1016/0956-716x(93)90572-a

Wang, Q., Lu, Y., Yu, Q., and Zhang, Z. (2018). The exceptional strong face-centered cubic phase and semi-coherent phase boundary in a eutectic dual-phase high entropy alloy AlCoCrFeNi. *Sci. Rep.* 8, 1–7. doi:10.1038/s41598-018-33330-0.

Wegrelius, L., Falkenberg, F., and Olefjord, I. (1999). Passivation of stainless steels in hydrochloric acid. *J. Electrochem. Soc.* 146, 1397–1406. doi:10.1149/1.1391777

Yasakau, K. A., Zheludkevich, M. L., Lamaka, S. V., and Ferreira, M. G. S. (2006). Mechanism of corrosion inhibition of AA2024 by rare-earth compounds. *J. Phys. Chem. B* 110, 5515–5528. doi:10.1021/jp0560664

Zhang, X. L., Jiang, Z. H., Yao, Z. P., Song, Y., and Wu, Z. D. (2009). Effects of scan rate on the potentiodynamic polarization curve obtained to determine the Tafel slopes and corrosion current density. *Corros. Sci.* 51, 581–587. doi:10.1016/j.corsci.2008.12.005

Zhang, Y., Zuo, T. T., Tang, Z., Gao, M. C., Dahmen, K. A., Liaw, P. K., et al. (2014). Microstructures and properties of high-entropy alloys. *Prog. Mater. Sci.* 61, 1–93. doi:10.3390/ma1203037010.1016/j.pmatsci.2013.10.001

Conflict of Interest: The authors declare that the research was conducted in the absence of any commercial or financial relationships that could be construed as a potential conflict of interest.